RSC Advances

PAPER

View Article Online
View Journal | View Issue

Cite this: *RSC Adv.*, 2026, **16**, 21613

Borate bioglass-incorporated xanthan hydrogel as an effective hemostat

Vanshika Singh,†[a] Marvaan M. S.,†[a] Vishwa S.,[a] Balashanmugan Panneerselvam[b] and G. Devanand Venkatasubbu *[a]

Received 3rd January 2026
Accepted 26th March 2026

DOI: 10.1039/d6ra00042h

rsc.li/rsc-advances

Hemostasis is an important part of surgical operations and trauma and wound care, and it prevents bleeding in three stages: vasoconstriction, platelet plug formation and coagulation. Borate bioglass (BBG) is a biocompatible material used in bone regeneration and repair. In borate bioglass-incorporated hemostasis hydrogels, the clotting process is facilitated by the release of ions such as boron, calcium, and sodium. The ions play a significant role in the coagulation cascade and are important in promoting platelet adhesion. Such hydrogels are biocompatible and biodegradable, which makes them ideal candidates for hemostatic applications. Herein, we synthesized borate bioglass nanoparticles and characterized them by XRD, FTIR spectroscopy, zeta potential measurements, and TEM. Antibacterial investigations demonstrated the good inhibition ability of these nanoparticles against wound pathogens. Blood clotting time analysis, blood clot index, RBC aggregation, PT and aPTT, D dimer assay, platelet aggregation, thrombus weight and hemolysis assay are done for borate bioglass. A BBG-incorporated xanthan hydrogel exhibited a remarkable hemostatic property, as demonstrated by *in vivo* analysis, with a blood clotting time of 90 s in a liver model, 164 s in a tail amputation model, and 211 s in a femoral artery model.

1 Introduction

Blood is a fascinating and functional connective tissue composed of plasma, red blood cells (RBC), white blood cells (WBC), and platelets, which are critical for homeostatic processes, nutrient delivery, immune defense, thermoregulation, and other vital functions. Among its essential functions for survival, the ability of blood to respond to vascular injury is essential for immediate life preservation through hemostasis. Hemostasis is a controlled, physiological, and dynamic response to the loss of vascular integrity. Hemostasis is composed of three overlapping phases, namely, vasoconstriction, primary hemostasis, and secondary hemostasis, culminating in stable fibrin clot formation.[1]

Vasoconstriction is the beginning of the hemostatic cascade. It is a reflexive contraction of smooth muscles around blood vessels, causing narrowing of the blood vessels. Vasoconstriction occurs due to the contraction of smooth muscles and release of bioactive molecules, such as endothelin-1, thromboxane A_2 (TXA_2), and serotonin, typically released from activated platelets. It minimizes blood loss and allows for the subsequent assessment of vascular irritability and recruitment of cellular and molecular hemostatic components for hemostasis. With vasoconstriction underway, the primary hemostasis process proceeds with the initial adhesion of platelets to subendothelial matrix proteins (collagen and von Willebrand factor) through glycoprotein Ib (GpIb) receptors. Platelet adhesion induces platelet activation, phospholipid exposure, changes in platelet morphology, and the release of procoagulant materials, including adenosine diphosphate (ADP), serotonin, and fibrinogen, leading to a transient platelet plug.[2,3]

Secondary hemostasis strengthens this temporary plug *via* the activation of the coagulation cascade involving the sequential conversion of zymogens to enzymes. The coagulation cascade can be initiated *via* an extrinsic pathway, activated by the tissue factor (TF) exposed at the sites of injury, or the intrinsic pathway, which begins when blood touches a negatively charged surface (subendothelial collagen). Both pathways converge to generate thrombin, which is a key protease that converts soluble fibrinogen into insoluble fibrin, which then cross-links to produce a durable clot.[4–6]

Apart from clot formation, thrombin enhances its own generation by activating factors V, VIII, XI and XIII, and promotes wound repair by facilitating the release of protease-activated receptors (PARs) from endothelial cells. The fibrin mesh formed and stabilized by factor XIIIa is tightly regulated by several anticoagulant systems, including antithrombin III, the protein C pathway, and tissue factor pathway inhibitor

---

[a] *Department of Physics and Nanotechnology, SRM Institute of Science and Technology, Kattankulathur, Chengalpattu District, Tamil Nadu, 603203, India. E-mail: gdevanandvenkatasubbu@gmail.com*

[b] *Avigen Biotech Pvt Ltd, Chennai, Tamil Nadu, India*

† Equal contribution.

(TFPI), to localize the response so that it does not progress to pathological thrombosis.[7,8] Following the restoration of vascular integrity, fibrinolysis begins, whereby plasminogen is converted to plasmin and causes the degradation of the clot into soluble fibrin degradation products, thereby completing the hemostatic cycle.[9]

Research has persistently examined biomaterials to imitate or expedite the natural hemostasis process in patients, especially in emergency medicine, surgical intervention, or battlefield medicine. Although suboptimal in pre-hospital conditions and trauma, current options, such as the placement of gauze or fibrin sealants, in addition to oxidized cellulose, fixation, compression, and tourniquets, all have basic hemostatic limitations, particularly in coagulopathic patients, without providing antimicrobial protection and providing appropriate dermal excipients and tissue regeneration support.[10]

To mitigate the limitations and the restrictive medical/surgical patient management need for hemostatic materials, there have been advances in borate-functionalized bioactive glasses (BBGs) for their dual hemostatic and therapeutic efficiency. Originally developed by Hench, the silica glass system was modified by exchanging silica with boron, increasing bioactivity and solubility. Unlike silicate-based bioglass, borate bioglass exhibits higher solubility due to the presence of trigonal BO_3 units, which readily hydrolyse under physiological conditions. The rapid ion release (Ca^{2+}, Na^+, and borate species) directly influences coagulation cascades, platelet activation, and fibrin formation. Understanding how these chemical features translate into biological performance is critical for rational hemostatic material design. Upon wound inspection, BBG quickly dissolves in body fluids, releasing a variety of ions, mainly calcium, boron, sodium and several other ions that accelerate coagulation, promote platelet activation, and initiate tissue mineralization and angiogenesis. BBG can potentially reduce bleeding time, benefit fibroblast proliferation, and accelerate wound closure, all of which are of tremendous interest for potential bioactive dressings and/or implants.[11–16]

However, BBG in its solid state does not have adequate mechanical integrity or flexibility for large and irregular wound areas. The BBG-incorporated hydrogel matrix offers a moist, flexible, and conformable scaffold for wound management. Hydrogels emulate a natural extracellular matrix, are injectable and have other properties, including biocompatibility and biodegradability or controllable degradation. Many biopolymers have been examined for hydrogel formulation, with xanthan gum being an interesting option, given its shear-thinning properties, thickening ability and biodegradability. Xanthan gum is produced from sugar fermentation by the *Xanthomonas campestris* bacteria. Xanthan gum forms a safe and stable gel at low concentrations, retains moisture near the wound, and has excellent film-forming properties.[17,18] Despite the potential topical biopolymer properties of xanthan gum, its ability to promote hemostasis with direct effects would be limited. Regardless, the underlying rationale for combining BBG with xanthan gum is that they work together: BBG bioactivity is ion-mediated with clot stimulation; xanthan gum provides a structural matrix, primarily to keep the glass particles at the injury site, and for greater controllable retention and release, adhesion and mechanical cohesion. The combination forms a multifunctional hemostatic hydrogel that can conform to wound surfaces, promote clotting under cellular activity, and resist microbial invasion.[19,20]

In this study, we propose that adding inorganic nanocomponents to the polysaccharide-based hydrogel will improve haemostatic function by speeding clotting, enhancing blood cell adhesion, and promoting rapid tissue sealing, without compromising biocompatibility. This study examines the hydrogel's structure–function relationship and assesses its haemostatic effectiveness using *in vitro* and *in vivo* models.

2 Materials and methods

Laboratory-grade xanthan gum ($C_{35}H_{49}O_{29}$), sourced from Sisco Research Laboratory Pvt. Ltd, possesses a molecular weight of 1000–2000 kDa and maintains a neutral pH of 7. The compound contains 1.5% pyruvic acid and demonstrates a viscosity of 600 mPa s at 25 °C. Its primary monosaccharide constituents—D-glucose, D-mannose, and D-glucuronic acid—are present in a 2 : 2 : 1 ratio.

2.1 Synthesis of borate bioglass

The sol–gel synthesis method was used, wherein 5 g of boric acid (H_3BO_3) was added to 100 mL of distilled water and after 2 h, 2.55 g of calcium chloride ($CaCl_2$) was added. After stirring for 2 h, the beaker was covered with aluminium foil and kept undisturbed at room temperature for 7 days. The samples were dried at 120 °C for 36 h, then calcined at 750 °C for 2 h with a heating rate of 2 °C min^{-1}.

2.2 Preparation of hydrogel

The hydrogel was prepared using xanthan gum ($C_{35}H_{49}O_{29}$). Three different concentrations (1%, 2% and 4%) of xanthan gum were prepared; 2% xanthan gum had the optimum viscosity, and it was incorporated with different concentrations of BBG (20, 40, 80, and 100 mg mL^{-1}). These concentrations were then added and thoroughly mixed to create a homogenous and cohesive hydrogel.

2.3 Inversion analysis

Inversion testing was carried out over a period of 5 days. The material was kept at the bottom of the vial, and the vial was then turned upside down and kept undisturbed to check the viscosity of the material.[21]

2.4 Spreadability analysis

Spreadability test was conducted to determine whether the prepared hydrogel could be easily spread and uniformly applied. Here, 1 g of hydrogel was placed between two glass plates (7 cm × 7 cm) and a standard weight of about 100 g was placed on top of the upper glass plate for 60 s. The spreadability (S) calculation is done using the following formula:

$$S = \frac{M \times L}{t}$$

where M = weight placed on the upper glass slide, L = length in cm, and T = time in seconds.

2.5 Injectability analysis

The hydrogel was taken in a syringe without air bubbles and pushed out to determine its flexibility. The hydrogel was pushed out by applying pressure to the back of the syringe. The smoothness with which the hydrogel escapes the syringe indicates its flexibility.

2.6 Swelling analysis

Swelling analysis was done to assess the fluid uptake capacity and structural stability with time. The weighed and dried hydrogel samples of 1 g were immersed in PBS (Phosphate Buffered Solution) at 37 °C. Every 2 h, the samples were removed, generally blotted to remove surface moisture and reweighed to calculate the swelling ratio. The swelling ratio (Q_0) was calculated using the following standard formula:[22]

$$Q_0\% = W_s - W_d/W_d \times 100$$

where W_s is the weight of the swollen hydrogel and W_d is the weight of the dry hydrogel.

2.7 Degradation analysis

For degradation analysis, the hydrogel was monitored over extended periods of time to observe weight loss, indicating material breakdown. The degradation ratio (Q_0) was calculated using the same formula used to find the swelling ratio.[22]

$$Q_0\% = W_s - W_d/W_d \times 100$$

where W_s is the weight of the swollen hydrogel and W_d is the weight of the dry hydrogel.

3 Antibacterial study

3.1 Antimicrobial activity

BBG was tested for its antimicrobial activity against two Gram-negative (*Escherichia coli* and *Pseudomonas aeruginosa*) and two Gram-positive (*Enterococcus faecalis* and *Staphylococcus aureus*) bacteria. The bacteria were kept for incubation in a nutrient broth medium. Agar plates were prepared and wells with a diameter of 4 mm were made. A bacterial inoculum of 100 µL was spread on the plate using an L-rod. BBG concentrations of 10, 20, 40 and 80 mg mL^{-1} were added to each labelled well and incubated at 37 °C for 24 h and the zone of inhibition was measured.[23]

3.2 Growth curve for borate bioglass

The growth kinetics of the bacteria treated with BBG were studied. This test was carried out by adding 200 µL of bacteria and nanoparticles in various concentrations to 3 mL of nutrient broth with bacterial inoculum. The absorbance was measured at 600 nm every 2 h for 24 h of incubation.[24]

4 Blood studies

Whole blood was drawn from healthy volunteers into vacutainer tubes with 3.2% sodium citrate, following ethical approval from SRM Medical College Hospital and Research Centre, Kattankulathur (ECR/8901/INST/TN/2013/RR-19).

4.1 Clotting time

Normal clotting time tends to be from 5 to 15 min, depending on the size and depth of the injury. This is measured by using an inverted microscope. Here, 10 µL of blood was dropped on a glass slide and smeared. Then, 10 µL of BBG at concentrations of 10, 20, 40 and 80 mg mL^{-1} and 10 mg of hydrogel were mixed with the smeared blood and visualized under a microscope. This showed how quickly BBG and hydrogels were able to react with the blood and aid in the clotting of the blood.

4.2 Blood coagulation index (BCI%)

The BCI% is determined to assess the blood coagulation efficiency of the material. Here, 100 µL of blood was taken in a test tube and incubated at 37 °C, and then, 10 mg of BBG was added and incubated for an additional 5 min to permit any clot formation that might occur. Next, 10 mL of distilled water was added to the tube, and the solution was kept undisturbed at 37 ° C for 2 min. The absorbance of the solution was measured at 540 nm. Then the BCI % was calculated using the formula given below.[25] The experiment was conducted in triplicate.

$$\text{BCI}\% = \frac{\text{OD sample}}{\text{OD blank}} \times 100$$

where OD sample = absorbance of the synthesized sample and OD blank = absorbance of the blank sample.

4.3 RBC aggregation

RBCs were first diluted in 5% saline to create a uniform cell suspension. For the control, 200 µL of the RBC was mixed with normal saline and incubated at 37 °C for 5 min to allow natural aggregation to occur. After incubation, unaggregated RBCs were removed by washing the sample with normal saline, ensuring that only aggregated cells remained. These aggregated RBCs were then lysed using 300 µL of 1% Triton X-100 for 5 min, which released intracellular hemoglobin into the solution. The absorbance was taken at 540 nm. RBC aggregation was calculated using the formula given below.[26] The experiment was conducted in triplicate.

$$\text{RBC aggregation } \% = \frac{\text{OD sample}}{\text{OD control}} \times 100$$

where OD sample = absorbance of the sample at 540 nm and OD control = absorbance of the control at 540 nm.

4.4 Prothrombin time (PT) and activated partial thromboplastin time (aPTT) assay

To evaluate the efficiency of the intrinsic and extrinsic coagulation pathways, PT and aPTT were determined. In this experiment, 200 µL of platelet-poor plasma was incubated with hydrogel and borate bioglass at 37 °C for 2 min; 100 µL of plasma was used in PT analysis. For aPTT, the same amount of plasma was used, mixed with 50 µL of aPTT reagents, and incubated for 3 min. Here, 0.025 M of 50 µL $CaCl_2$ was added to trigger clotting and the time was noted.[27] The experiment was conducted in triplicate.

4.5 D-dimer assay

In this experiment, plasma was separated from the blood and treated with hydrogel and borate bioglass at different concentrations. The plasma was treated with hydrogel and BBG and was analyzed using a coagulation analyzer. The experiment was conducted in triplicate.

4.6 Platelet aggregation

A lactose dehydrogenase (LDH) assay kit was used to assess platelet aggregation. BBG nanocomposites at different concentrations were incubated with platelet-rich plasma (PRP) (200 µL) for 5 min in a 48-well plate. Unaggregated platelets were washed with saline, whereas the aggregated platelets were lysed with the addition of 300 µL of 1% Triton X-100. The lysed material was recovered after 1 h of incubation. It was then analyzed with the LDH kit, and the platelet aggregation was measured at 490 nm.[28] The experiment was conducted in triplicate.

4.7 Thrombus weight

An equal amount of whole blood was added to all vials. The blood was treated with hydrogel and borate bioglass and left undisturbed until it clotted. The weight of the clotted blood was measured and separated from the empty vial to determine the thrombus weight. Before the addition of the blood, the empty vials were weighed. The following formula was used to calculate the thrombus weight. The measurements were done in triplicates.[29]

$$\text{Thrombus weight (g)} = \text{weight of vial with blood} - \text{weight of vial without blood}$$

4.8 Hemolysis assay

Hemolysis analysis was done to evaluate the potential of the test material to cause RBC membrane damage and subsequent lysis. Blood was subjected to centrifugation at 4000 rpm for 5 min to isolate the plasma. The plasma was then extracted. The blood cells were then washed two times with PBS to remove residual plasma components, and the supernatant was discarded after each wash. The isolated RBCs were then resuspended in 0.9% saline (PBS). A positive control was prepared to represent 100% hemolysis, consisting of RBCs treated with a few microliters of Triton X-100, which is a detergent known to fully disrupt cell membranes. The negative control, indicating 0% hemolysis, consisted of RBCs suspended only in saline solution. Following incubation, the samples were centrifuged, and the absorbance of the supernatant was measured at 545 nm using a UV-Vis spectrophotometer.[30] The hemolysis percentage was calculated using the formula below. The experiment was conducted in triplicate.

$$\text{Hemolysis } \% = \frac{\text{OD sample} - \text{OD negative}}{\text{OD positive} - \text{OD negative}} \times 100$$

where OD sample = absorbance of the synthesized sample, OD negative = negative control absorbance, and OD positive = positive control absorbance.

4.9 MTT assay (cell viability)

The MTT assay was conducted to check the biocompatibility of the material. The samples first underwent a thorough washing and sterilization process using ethanol for 30 min. They were then exposed to DMEM (Dulbecco's Modified Eagle's Medium) containing 10% FBS (Fetal Bovine Serum) for a duration of 12 h. After incubation, the medium was removed, and freshly cultured fibroblast cells were seeded into the samples at a density of 1×10^5 cells and incubated for 3 days. After this culturing period, the medium was aspirated and each well received 200 µL of a 0.05% MTT solution, which was left to incubate for 2 h at a temperature of 37 °C. To dissolve the resulting formazan crystals, DMSO (dimethyl sulfoxide) was added, and the OD (optical density) was measured at 570 nm.[31]

5 Animal studies

This study was conducted according to the established guidelines and received approval from the Institutional Animal Ethical Committee (IAEC). Four groups of six male Wistar rats, each weighing 180–240 g, were used as models. Both male and female animals were included in the analysis to validate coagulation responses.

5.1 Experimental animals

Group 1 served as the untreated control, and group 2 was the positive control, which was treated with the commercial drug etamsylate (standard). Groups 3 and 4 were treated with hydrogels A (pure xanthan hydrogel) and B (BBG xanthan hydrogel), respectively. Rats were housed in polypropylene cages. The diet consisted of pellet feed, and the animals were accommodated on bedding made from sterile paddy husk. The animals were grouped into positive, negative and 3 treatment groups with each group consisting of 6 animals.

5.2 *In vivo* blood clotting assessed by tail amputation

The tails of anesthetized albino rats were sterilized using 75% alcohol to increase the blood flow. The tails were amputated and bleeding was observed for 15 S before the hydrogels were introduced at the bleeding site. The time taken for bleeding to cease was meticulously recorded. The blood loss was assessed by collecting surplus blood using standard medical gauze, which was then weighed.[32]

5.3 *In vivo* blood clotting assessed by liver incision

The Wistar rats were anesthetized and their abdominal area was shaved and sterilized with 70% alcohol. A precise incision was made in the abdominal cavity, and a section of liver was excised to generate a wound of approximately 0.5 cm in length, leading to spontaneous bleeding for 5 s. The blood was carefully removed with gauze, and the sample was applied delicately to the wound. The observations were made to monitor the bleeding status of the wounds and the precise moment the bleeding ceased was recorded. Any blood clots within the wound area were then absorbed using a gauze cloth.[33]

5.4 *In vivo* blood clotting assessed by femoral artery puncture

The Wistar rats were subjected to anesthesia. The thigh area was shaved and sterilized with 70% alcohol. The femoral artery was then identified and punctured using a 21G needle, resulting in bleeding that lasted for 5 s. The hydrogel samples were delicately applied to the wound. The bleeding status of the wound was monitored and the moment the bleeding ceased was recorded. Any clotted blood within the wound area was removed using a gauze cloth.[33]

5.5 Statistical analysis

The results are presented as mean ± standard deviation; experiments were conducted in triplicate (for *in vitro* studies, $n = 3$, and for *in vivo* studies, $n = 6$). A one-way ANOVA with GraphPad Prism 8.0 software was used for the statistical analysis, and $p < 0.05$ was statistically significant.

6 Results and discussion

6.1 Characterization

6.1.1 XRD analysis. The synthesised calcium borate bioglass XRD pattern exhibited multiple well-defined diffraction peaks, confirming the predominantly crystalline nature. The diffraction pattern exhibited several well-defined reflections that can be indexed to crystalline calcium borate phases in accordance with the reference pattern no. 01-083-2025, with the most intense peak observed at $2\theta \approx 29$–30°; the prominent diffraction peak observed at approximately $2\theta \approx 27$–28° corresponds to the (−212) plane and represents the most intense reflection of the calcium borate structure. Additional reflections located around 12–15°, 16–18°, 20–25°, and 30–45° can be indexed to the (110), (200), (111), (120), (021), (220), (112), (230), (330), (030), (−331), (−303), (−332), (−142), and (004) lattice planes, respectively, confirming the formation of a crystalline calcium borate phase along with several characteristic reflections in the low- and mid-angle regions. Minor variations in relative peak intensities and peak broadening were evident when compared with the reference pattern, which may arise from slight deviations in Ca/B stoichiometry and reduced crystallite size. The gradual reduction in diffraction intensity at higher angles and the presence of a weak, diffuse background suggest a limited degree of structural disorder. The observed diffraction features indicate the formation of calcium borate bioglass with long-range Ca–O–B ordering, while local structural distortions and non-ideal crystallinity are likely influenced by network-modifying Ca^{2+} ions and the synthesis conditions. Such ion release plays an important role in stimulating biological responses, including hemostasis, angiogenesis, and tissue regeneration. Therefore, the observed crystalline features in the BBG structure are expected to contribute to its bioactivity by providing a stable, yet ion-releasing framework. The incorporation of BBG and xanthan gum showed an amorphous peak near $2\theta \approx 20°$. The XRD results confirmed the successful formation of borate bioglass and incorporation of BBG into the xanthan gum matrix (Fig. 1).

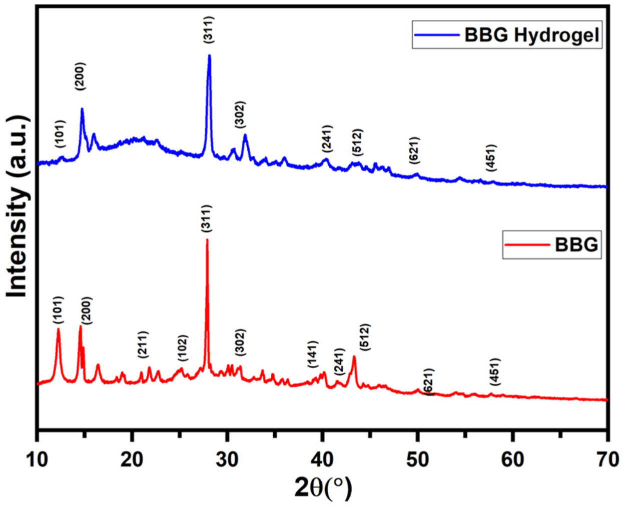

Fig. 1 XRD patterns of borate bioglass and the BBG-incorporated hydrogel.

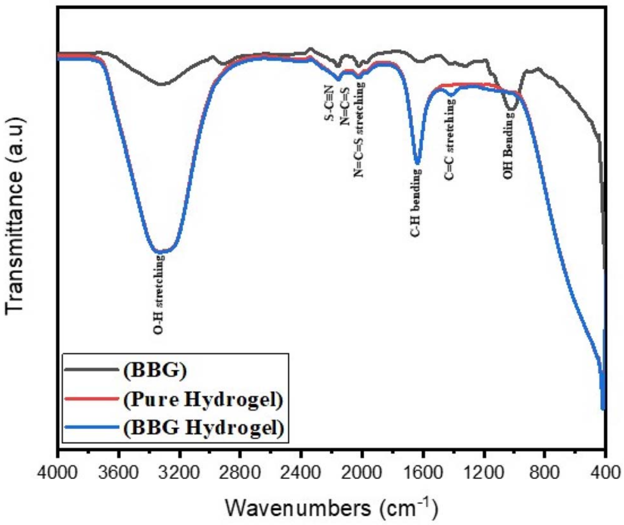

Fig. 2 FTIR spectra of BBG, pure hydrogel and BBG-incorporated hydrogel.

6.1.2 FTIR spectroscopy. The FTIR spectra (Fig. 2) of the borate bioglass show identifiable vibrational bands in the region of 1400–1600 cm^{-1} and broad bands in the regions of 3400 cm^{-1}, demonstrating the presence of –OH groups. This confirmed the hydrophilic nature of the borate bioglass. The peaks at 700–1100 cm^{-1} can be attributed to B–O–B and B–O–Ca linkages, suggesting calcium incorporation into the borate matrix. The presence of B–O–B and B–O–Ca linkages confirmed the formation of a chemically connected borate network, which facilitates rapid hydrolysis upon contact with blood. The retained hydroxyl groups contribute to hydrophilicity and promote protein adsorption, a critical first step in platelet adhesion and clot initiation. The FTIR spectrum of xanthan gum displays strong O–H stretching, C–O–C glycosidic vibrations, and carboxylate-associated bands characteristic of the polysaccharide backbone. Upon incorporation of BBG into the xanthan matrix, no new covalent bond peaks were observed; however, subtle changes in band intensity and slight broadening of the O–H and carboxylate-related regions were evident. These changes suggest the presence of ionic interactions and hydrogen bonding between released Ca^{2+}/borate species and the functional groups of xanthan gum, rather than the chemical degradation of the polymer backbone. The preservation of the major vibrational features confirmed that BBG incorporation does not disrupt the chemical integrity of the hydrogel while enabling ion-mediated interactions relevant to hemostatic and biological activity.

6.1.3 HRTEM analysis. The HRTEM image of BBG is shown in Fig. 3a, which indicates the morphology and microstructural characteristics of the synthesized calcium borate bioactive glass (BBG). The TEM image reveals irregular platelet-like nanoparticles with an average lateral dimension of approximately 40–80 nm. The particles appear slightly aggregated, which is typical for borate-based glass nanoparticles due to their high surface energy and interparticle interactions. The nanoscale particle size is advantageous for biomedical applications, as smaller particles provide a higher surface area that can facilitate faster ion exchange and dissolution behaviour in physiological environments. The selected area electron diffraction (SAED) pattern in Fig. 3b exhibits distinct diffraction rings composed of numerous bright spots, indicating the presence of polycrystalline domains within the BBG particles. The ring-like diffraction pattern suggests that the nanoparticles consist of multiple randomly oriented crystalline domains rather than a completely amorphous structure. This observation is consistent with the XRD results, which also indicated partial crystallinity in the material. Further structural insights were obtained from the high-resolution TEM (HRTEM) image in Fig. 3c, where well-resolved lattice fringes can be observed. The measured interplanar spacing of $d = 0.423$ nm corresponds to a characteristic lattice plane of crystalline calcium borate phases, further confirming the formation of ordered domains within the BBG nanoparticles. The coexistence of crystalline regions within a glass-derived borate network is commonly reported for

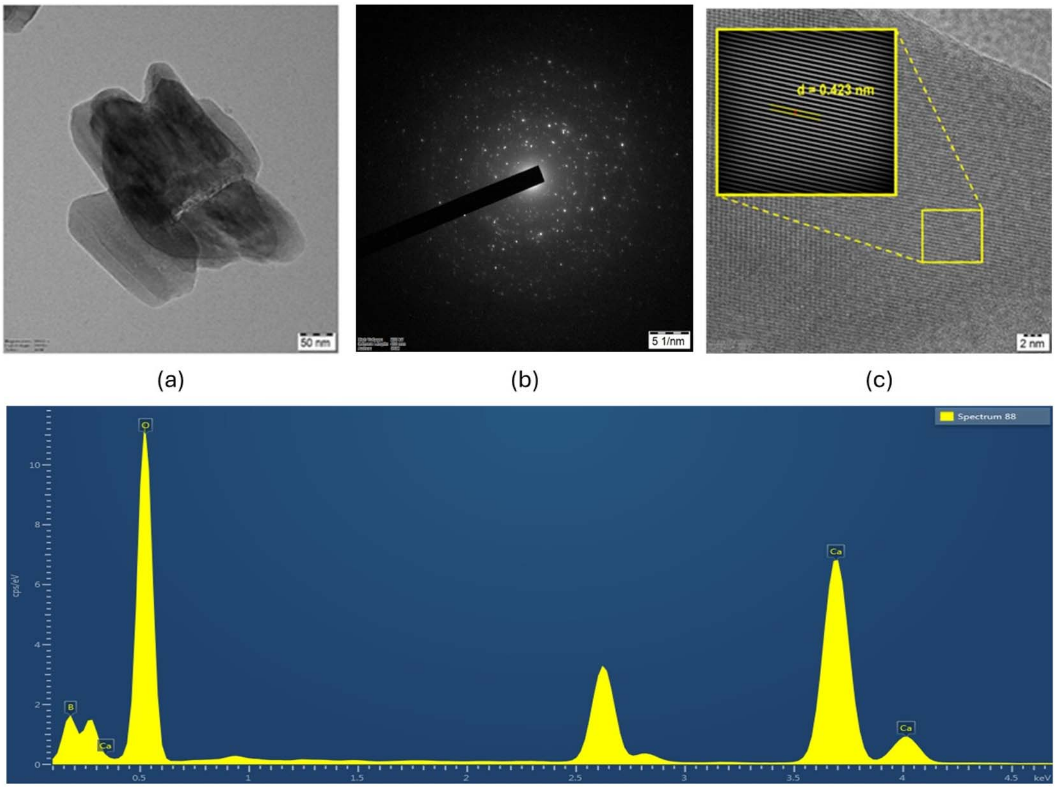

(a) (b) (c)

(d)

Fig. 3 (a) HRTEM image, (b) SAED pattern and (c) HRTEM image of the lattice plane. (d) EDS spectrum of BBG.

borate-based bioactive systems and arises from the relatively flexible borate structural units that can reorganize into ordered configurations during synthesis. Energy-dispersive X-ray spectroscopy (EDS) analysis in Fig. 3d confirms the elemental composition of the synthesized material, with characteristic signals corresponding to Ca, B, and O, which are the principal components of calcium borate bioactive glass. No additional impurity peaks were detected, indicating the chemical purity of the synthesized BBG. The nanoscale morphology and partially crystalline structure observed in the TEM analysis are expected to influence the biological performance of BBG. The high surface area associated with nanosized particles can enhance the dissolution kinetics of borate glasses, promoting the release of biologically active ions such as Ca^{2+} and borate species. These ions are known to play important roles in regulating biological responses, including coagulation, cell signalling, and tissue regeneration, which are essential for effective hemostatic performance.

6.1.4 Zeta potential analysis. The zeta potential values of BBG nanoparticles, pure xanthan hydrogel, and BBG-incorporated hydrogel are summarized in Table 1. BBG nanoparticles exhibit a moderately negative zeta potential (−11.1 mV), indicating limited electrostatic stabilization in aqueous suspension. This magnitude suggests that colloidal stability is not governed solely by electrostatic repulsion but also by short-range interactions and hydration effects, which is typical for bioactive glass systems. The pure xanthan hydrogel displays a similar negative surface potential (−10.7 mV), arising from the presence of ionized carboxylate groups along the polysaccharide backbone. Upon the incorporation of BBG into the hydrogel matrix, the zeta potential shifts slightly toward neutrality (−10.2 mV), likely due to partial charge screening by released Ca^{2+} ions and interactions between the glass surface and polymer chains. The moderately negative zeta potential (−10 to −11 mV) suggests the partial surface deprotonation of borate groups, enabling electrostatic interactions with positively charged domains of plasma proteins such as fibrinogen. Upon blood contact, ionic screening and protein adsorption are expected to reduce repulsion effects, allowing effective blood–material interactions despite the net negative charge. This will allow for electrostatic interaction with biological molecules (*e.g.*, proteins and RBCs). The BBG-incorporated hydrogel gives a similar negative zeta potential of −10.2 but a slight shift toward neutrality as shown in Table 1.

Table 1 Zeta potential of BBG and hydrogels

S. no.	Sample	Zeta potential (mV)
1	BBG	−11.1
2	Pure hydrogel	−10.7
3	BBG-incorporated hydrogel	−10.2

7 Hydrogel studies

7.1 Inversion test

The physical performances of the borate bioglass–xanthan gum hydrogels under both static and applied circumstances are presented in Fig. 4. Over the course of five days, the inversion test verified that the hydrogel based on 2% xanthan gum was sufficiently stable. This conforms to adequate gelation and structural integrity to maintain its shape. Its non-Newtonian, gel-like characterisation was confirmed throughout the test by the absence of either flow or separation. This is in line with other comparable thixotropic biological hydrogels.

7.2 Spreadability analysis

The spreadability of the hydrogel was assessed using a dual glass plate method. The hydrogel showed the best spreadability under applied weight, producing a flat, uniform layer with no evidence of fragmentation or rupturing. The viscosity was moderate, such that the material was thick enough to spread. However, it also had some structural continuity to prevent excessive flow. The hydrogel is spreadable (8.167 cm) and its spreadability characteristics support the material's topical application. This could be developed to further promote and facilitate wound healing and haemostasis. The spreadability of the BBG-incorporated hydrogel and the BBG-incorporated xanthan gum hydrogel (7.833 cm) is shown in Fig. 5a.

7.3 Injectability analysis

The injectability testing of the hydrogels is shown in Fig. 5b. For injectability, the hydrogel material was loaded into a standard syringe and extruded from the syringe using a manual compressive force. The material demonstrated a smooth, continuous flow from the syringe, with no clogging or phase separation, thus confirming its injectability. This also confirms

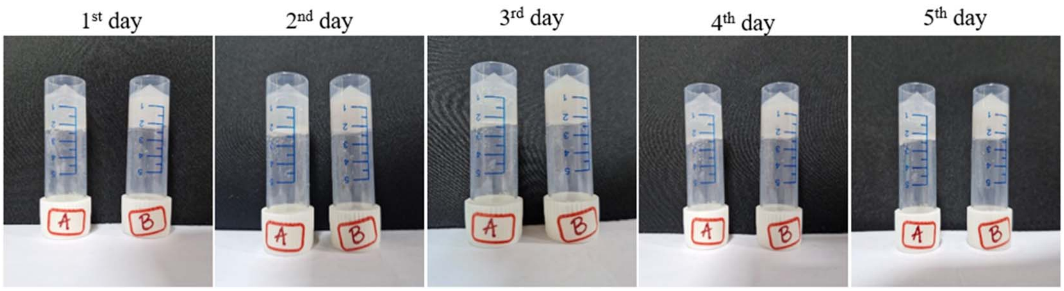

Fig. 4 Inversion analysis of hydrogels.

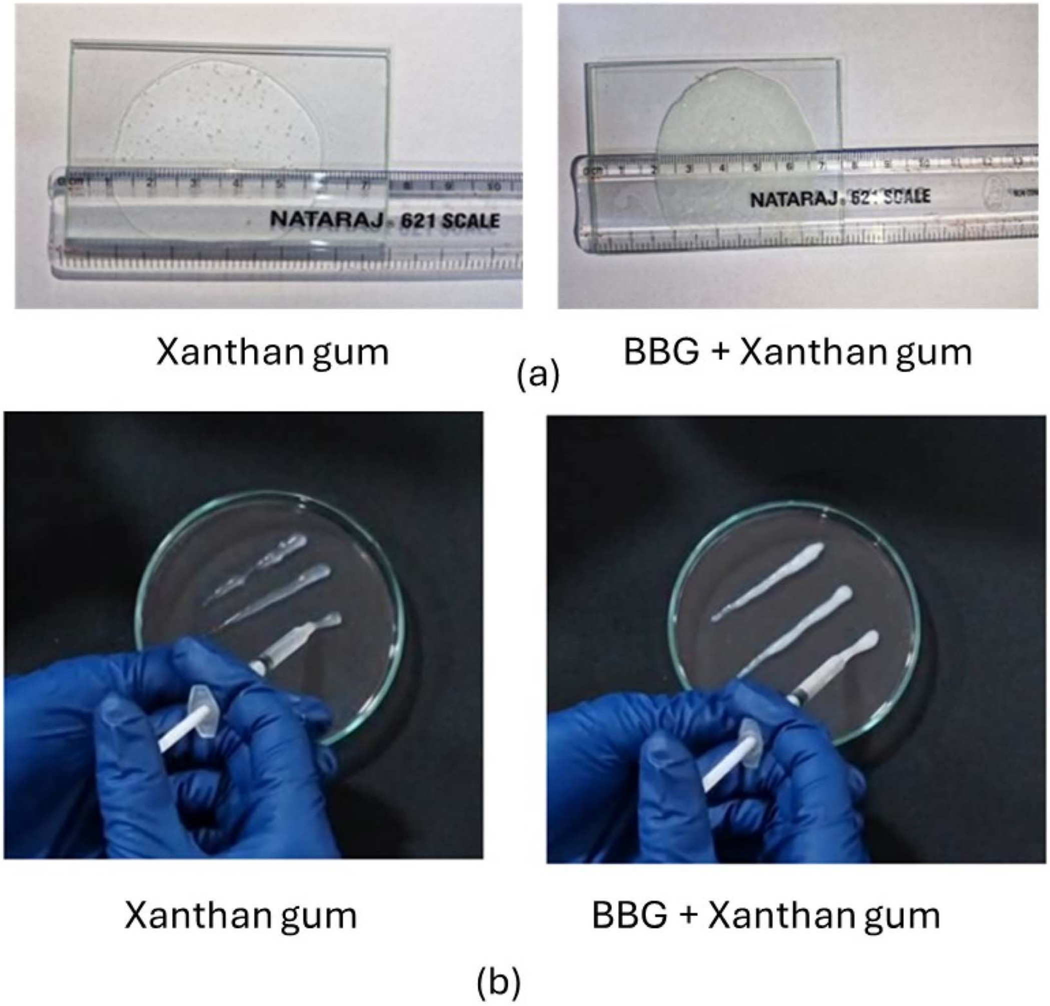

Fig. 5 (a) Spreadability of hydrogels. (b) Injectability analysis of hydrogels.

its existence as a shear-responsive material. This indicates its thixotropic properties, where phase viscosity is reduced with an applied stress, allowing for a smooth flow.

7.4 Swelling analysis

The swelling (Fig. 6a) behaviour of the pure hydrogel and the BBG-incorporated hydrogel. Within the initial hours, both hydrogels demonstrated a rapid increase in the swelling ratio,

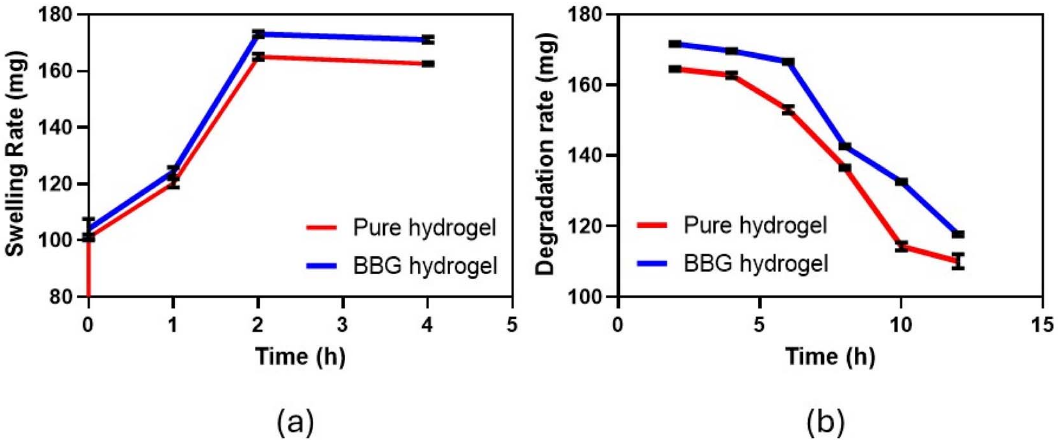

Fig. 6 (a) Swelling and (b) degradation analyses of hydrogels.

which reached its peak at approximately four hours. At each time interval, the BBG-incorporated hydrogel consistently exhibited a slightly higher swelling ratio than the pure hydrogel, indicating that it has a greater capacity to absorb water. The enhanced swelling of BBG-incorporated hydrogels can be attributed to increased osmotic pressure generated by ionic dissolution from the borate glass phase. This swelling facilitates rapid blood absorption and concentrates coagulation factors at the wound interface, thereby accelerating clot formation.

7.5 Degradation analysis

Fig. 6b shows the degradation behaviour upon reaching the peak; the swelling ratio of both hydrogels progressively decreased because of structural degradation. The BBG-incorporated hydrogel exhibited a slower decline than the purified hydrogel, which implies that it has superior structural stability and a slower rate of degradation. At 12 h, both hydrogels exhibited a significantly reduced swelling ratio; however, the BBG-incorporated hydrogel maintained a higher value than the pure hydrogel. The slower degradation of the BBG-containing hydrogels suggests ionic crosslinking effects between the released Ca^{2+} ions and xanthan gum chains, which reinforced the hydrogel network and prolonged functional integrity during hemostasis. This suggests that the hydrogel's water retention was improved, and its degradation was reduced by the incorporation of the BBG nanoparticles.

8 Microbial studies

8.1 Well diffusion

The antibacterial activity of the BBG nanoparticles is shown in Fig. 7. The zones of inhibition are presented in Table 2. BBG exhibited distinct antibacterial zones of inhibition against both Gram-negative (*E. coli*, *P. aeruginosa*) and Gram-positive (*S. aureus*, *E. faecalis*) bacteria. The level of inhibition increased with concentration (80 mg mL^{-1} exhibited the largest zone diameter). This could be due to the antibacterial activity of BBG.

Table 2 Zones of inhibition of BBG

Concentration of BBG (mg mL^{-1})	Zone of inhibition			
	P. aeruginosa	*E. coli*	*S. aureus*	*E. faecalis*
10	—	—	0.3 cm	—
20	—	—	0.4 cm	—
40	—	0.5 cm	0.4 cm	0.1 cm
80	0.2 cm	0.7 cm	0.6 cm	0.5 cm

8.2 Growth curve

The growth kinetics (Fig. 8) revealed that BBG exerts a strong, concentration-dependent antibacterial effect against all tested wound pathogens. For *S. aureus* (a), the control showed rapid exponential growth, while 20 and 40 mg mL^{-1} partially suppressed proliferation. At 80 mg mL^{-1}, growth was markedly reduced, and at 100 mg mL^{-1}, growth was completely inhibited throughout the 24 h, indicating potent bactericidal action. *P. aeruginosa* (b), a highly resilient Gram-negative pathogen, experienced moderate inhibition at 20 and 40 mg mL^{-1}, whereas 80 mg mL^{-1} significantly delayed exponential growth. Complete inhibition was observed at 100 mg mL^{-1}, demonstrating effective suppression of this typically drug-tolerant species.

The inhibition analysis revealed that BBG exhibited strong, concentration-dependent antibacterial activity against all tested wound pathogens. At 20 mg mL^{-1}, growth reduction remained moderate (26–42%), indicating partial metabolic suppression. Increasing the concentration to 40 mg mL^{-1} significantly enhanced inhibition, yielding 44–68% reduction depending on species. The most substantial inhibitory shift occurred between 40 and 80 mg mL^{-1}, where inhibition increased sharply to 73–91%, demonstrating that 80 mg mL^{-1} is a critical threshold for effective growth suppression. At 100 mg mL^{-1}, BBG achieved >93–98% inhibition across all pathogens, confirming near-complete bactericidal activity.

9 Hemostatic blood studies

9.1 Clotting time

The clotting times of BBG at different concentrations and the hydrogels are shown in Fig. 9a. The control group has the longest clotting time, which is approximately 6 min, indicating that the clot is forming slowly. In comparison to the control group, all treated groups exhibited a substantial reduction in coagulation time. The coagulation time was reduced to

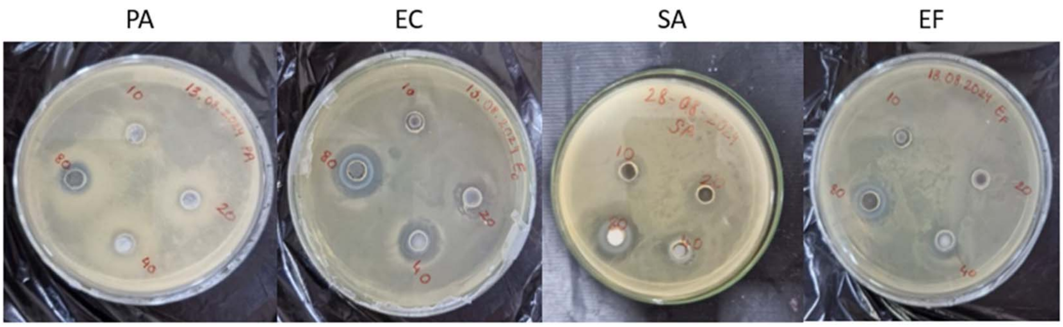

Fig. 7 Zones of inhibition of BBG.

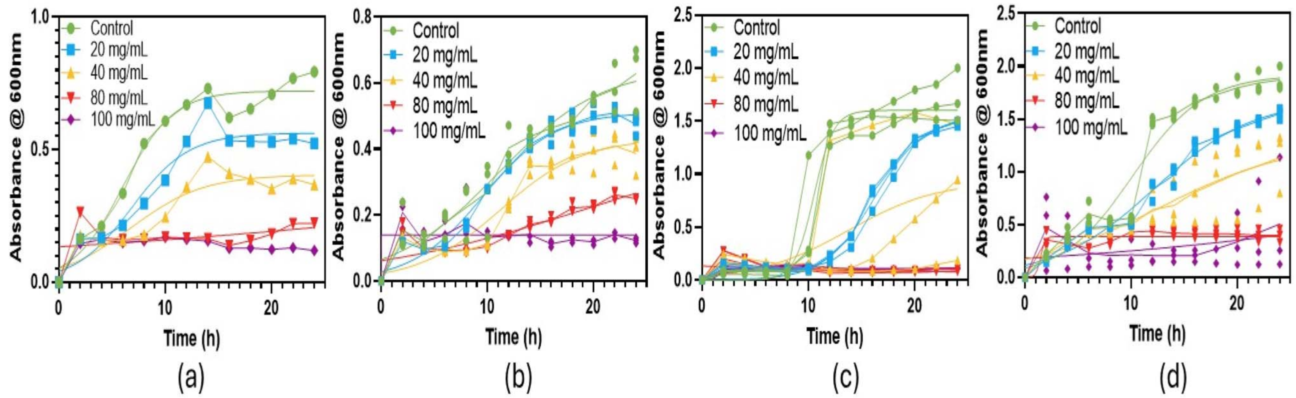

Fig. 8 Growth curves of BBG-treated (a) *S. aureus*, (b) *P. aeruginosa*, (c) *E. coli* and (d) *E. faecalis*.

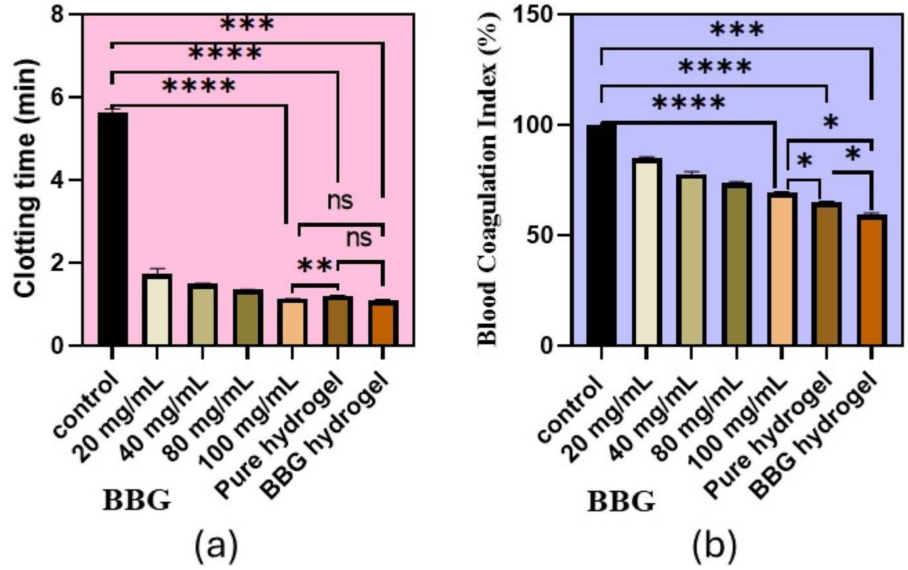

Fig. 9 (a) Clotting time and (b) blood coagulation index of BBG and hydrogels. Error bars represents SD for $n = 3$, *** represents $P < 0.0001$, *** represents $P = 0.001$, ** represents $P = 0.01$, and * represents $P < 0.1$.

approximately 2.2 min in the 20 mg mL^{-1} group, and it was further reduced to approximately 1.8 min in the 40 mg mL^{-1} group. Similarly, the 80 mg mL^{-1} and 100 mg mL^{-1} groups exhibited coagulation times of approximately 1.6–1.7 min, with no statistically significant difference between them (ns). The pure hydrogel exhibited a slightly shorter clotting time (∼1.5 min), while the BBG-incorporated hydrogel showed the shortest clotting time (∼1.3 min), which is significantly faster than the pure hydrogel ($p < 0.01$). This trend suggests that the coagulation time decreases in a concentration-dependent manner up to 40 mg mL^{-1} and reaches a plateau. The clotting time assay showed that both the xanthan hydrogel and BBG-containing formulations significantly reduced coagulation time compared to the control. The pure xanthan hydrogel exhibits strong haemostatic activity due to its rapid fluid absorption and ability to concentrate blood components. The incorporation of BBG resulted in a moderate additional reduction in clotting time (∼10–15 s), which may be attributed to the release of Ca^{2+} ions that participate in the coagulation cascade. The accelerated clotting observed for BBG-incorporated hydrogels arises from a combination of chemical and physicochemical effects: rapid Ca^{2+} release enhances thrombin generation, borate-mediated platelet activation, then surface charge-driven protein adsorption, and finally, hydrogel-mediated blood concentration at the wound site. These synergistic mechanisms explain the superior performance compared to the pure hydrogel and BBG alone. The most potent haemostatic effect was exhibited by the BBG-incorporated hydrogel.

9.2 Blood coagulation index (BCI)

The BCI of different concentrations BBG and the hydrogel is given in Fig. 9b. The control exhibited the highest BCI (approximately 100%). The 20 mg mL^{-1} group exhibited a modest reduction in BCI (∼85%), whereas the 40 mg mL^{-1} and 80 mg mL^{-1} groups exhibited even greater reductions

($\sim$75% and $\sim$70%, respectively). The pure hydrogel exhibited a BCI of approximately 60%, while the 100 mg mL^{-1} group exhibited a BCI of approximately 65%. The BBG-incorporated hydrogel had the lowest BCI of approximately 55%. In comparison to all other groups, the BBG-incorporated hydrogel significantly reduced BCI ($p < 0.05$), suggesting greater coagulation efficiency. The BCI assay further confirmed the clot-forming ability of the materials. The BBG-incorporated hydrogels showed lower BCI values compared to the pure xanthan hydrogel, indicating improved clot formation efficiency. However, the difference was modest, suggesting that the haemostatic behaviour arises mainly from the combined additive effects of the xanthan matrix and BBG particles.

9.3 Red blood cell aggregation assay

Fig. 10a shows the RBC aggregation by BBG and BBG-incorporated xanthan gum. The RBC aggregation assay indicates a concentration-dependent increase in RBC aggregation with borate bioglass and xanthan gum hydrogel. In the BBG, greater RBC aggregation, specifically at 80 mg mL^{-1} and 100 mg mL^{-1}, was observed compared to the control. This indicates sufficient interaction with erythrocytes in the earlier stages of clot formation. The control group exhibited minimal RBC aggregation, whereas the 20 mg mL^{-1} and 40 mg mL^{-1} groups exhibited moderate aggregation. The rate of aggregation further increased at 80 mg mL^{-1} and 100 mg mL^{-1}. The BBG-incorporated hydrogel exhibited the highest aggregation. RBC aggregation studies revealed that the xanthan hydrogel promoted erythrocyte clustering due to its viscous network and fluid absorption capacity. The incorporation of BBG produced an increase in RBC aggregation, likely influenced by the ionic environment created by the borate glass particles.

9.4 Platelet aggregation assay

The platelet adhesion is shown in Fig. 10b. For BBG, in a concentration dependent manner, the platelet adhesion increased gradually from 20 mg mL^{-1} to 100 mg mL^{-1}. The maximum platelet adhesion was exhibited by the BBG-incorporated hydrogel, which was substantially higher than for all groups. Platelet aggregation studies showed that both the pure xanthan hydrogel and BBG-containing composites supported effective platelet attachment on the material surface. The xanthan hydrogel itself facilitated platelet aggregation due to its hydrated polymeric network, which can physically entrap platelets and concentrate coagulation factors at the interface. Upon the incorporation of BBG, an increase in platelet aggregation was observed. This behaviour may be attributed to the presence of inorganic particles and the gradual release of Ca^{2+} ions, which play an essential role in platelet activation and aggregation during the coagulation process. In addition, the nanoscale surface features introduced by BBG particles may provide favourable sites for platelet attachment. However, the difference between the pure hydrogel and BBG-containing formulations remained moderate, suggesting that platelet interaction is primarily governed by the hydrogel matrix, with BBG contributing an additional supportive effect.

9.5 Prothrombin time and activated partial thromboplastin time (PT and aPTT)

The PT and aPTT values for BBG and the BBG-incorporated hydrogel are given in Fig. 11a and b. The PT and aPTT assays showed that clotting times for both tests were shorter with the BBG-incorporated hydrogel. The PT values dropped from 22–37 s (normal) to $\sim$15 s and aPTT from 12–15 s to $\sim$9 s, confirming that BBG can activate both the extrinsic and intrinsic coagulation pathways. The control group had the highest PT ($\sim$15 s) value, which suggests delayed initiation of the clot. The PT was progressively shortened as the concentration increased from 20 mg mL^{-1} to 100 mg mL^{-1}, indicating improved coagulation. The 20 mg mL^{-1} group exhibited a modest but significant reduction, whereas the 40 mg mL^{-1} and 80 mg mL^{-1} groups showed greater reduction. The 100 mg mL^{-1} group exhibited an additional decrease, comparable to that of 80 mg

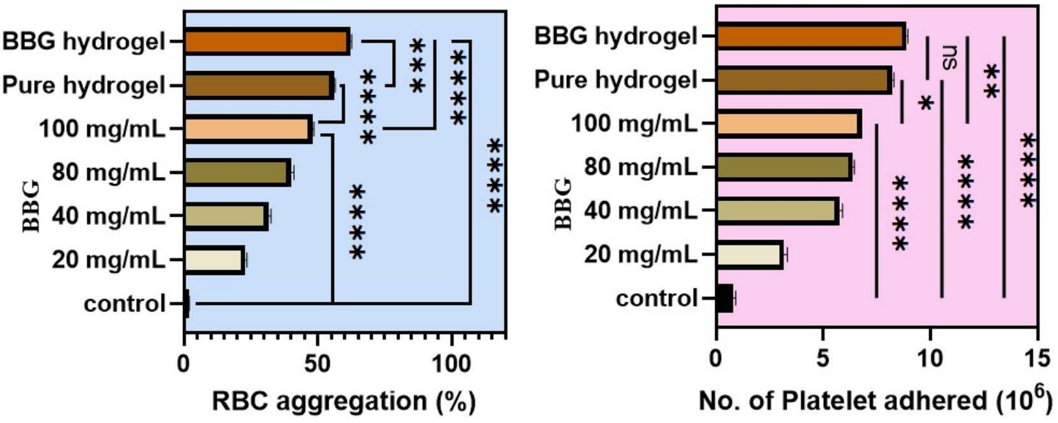

(a) (b)

Fig. 10 (a) RBC aggregation and (b) platelet adhesion of BBG and hydrogels. Error bars represents SD for $n = 3$, *** represents $P < 0.0001$, *** represents $P = 0.001$, ** represents $P = 0.01$, and * represents $P < 0.1$.

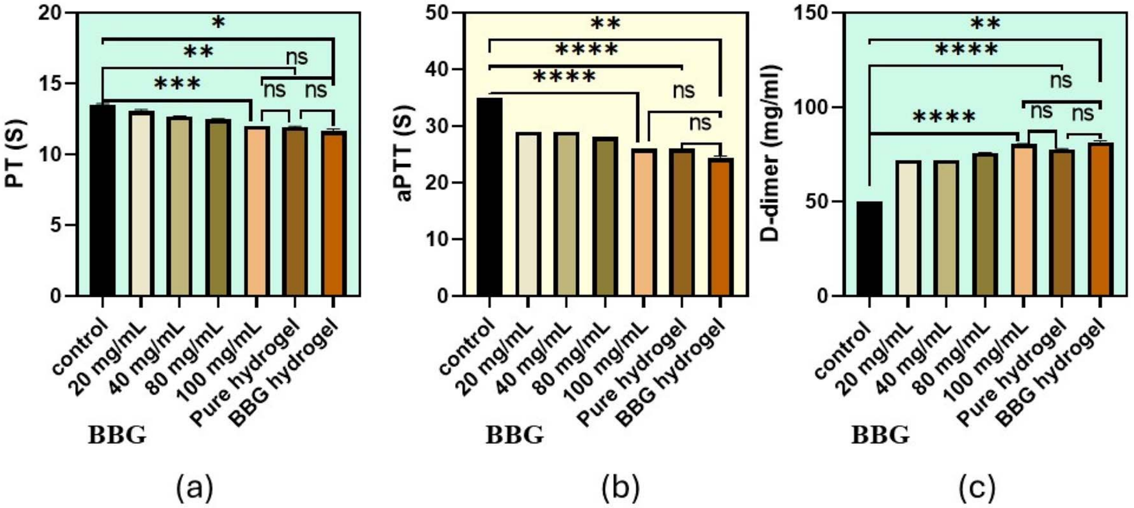

Fig. 11 (a) Prothrombin time, (b) activated partial thromboplastin time and (c) the D-dimer levels of BBG and hydrogels. The error bars represent SD for $n = 3$, *** represents $P < 0.0001$, *** represents $P = 0.001$, ** represents $P = 0.01$ and * represents $P < 0.1$.

mL^{-1}. Both the pure hydrogel and BBG-incorporated hydrogel exhibited the lowest PT values, which were substantially lower than the control but not significantly different from each other (ns). This suggests a robust procoagulant effect.

In aPTT, the control group exhibited the highest aPTT (~36 s) value, indicating delayed activation of the intrinsic pathway. The aPTT decreased continuously as the concentration increased. The 20 mg mL^{-1} group exhibited a substantial decrease (**), while the 40, 80, and 100 mg mL^{-1} groups exhibited even greater decreases (****), indicating that clot formation occurred at a rapid pace. In comparison to the control, the pure hydrogel and BBG-incorporated hydrogel exhibited the lowest aPTT values (ns), which were substantially reduced but not significantly different from each other. This confirms the enhanced intrinsic coagulation activity.

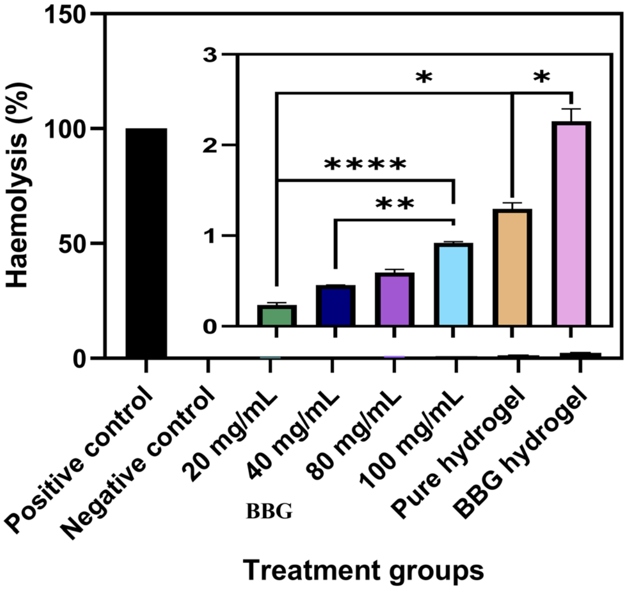

Fig. 12 Hemolysis of BBG and hydrogels. The error bars represent SD for $n = 3$, *** represents $P < 0.0001$, *** represents $P = 0.001$, ** represents $P = 0.01$ and * represents $P < 0.1$.

10 D dimer assay

The D-dimer analysis is given in Fig. 11c. Suggested D-dimer values conform to the clot formation without an excessive amount of fibrinolysis. Platelet aggregation indicated massive aggregation with increasing levels of BBG concentration that resulted from the ability of the borate ions to activate platelets. The control group exhibited the lowest D-dimer levels (approximately 50 μg mL^{-1}). D-dimer levels exhibited a modest increase at 20 mg mL^{-1} and 40 mg mL^{-1}, and more significant increases at 80 mg mL^{-1} and 100 mg mL^{-1} (****), indicating increased fibrin formation and breakdown at higher concentrations. The pure hydrogel and BBG-incorporated hydrogel exhibited the highest D-dimer levels, which were substantially higher than the control but not significantly different from each other (ns). This suggests that the hydrogels can form clots with associated fibrinolysis.

11 Hemolysis assay

The haemolysis analysis of BBG and hydrogel is presented in Fig. 12. The results are presented as percentage hemolysis relative to positive and negative controls. The positive control shows complete erythrocyte lysis with approximately 100% hemolysis, while the negative control exhibits negligible hemolysis, confirming the reliability of the assay. The nanomaterial dispersions demonstrate very low hemolytic activity across the tested concentrations. The hemolysis percentage was approximately 0.18%, 0.35%, 0.55%, and 0.92% for 20, 40, 80, and 100 mg mL^{-1}, respectively, indicating a slight concentration-dependent increase but remaining well below the acceptable limit. For the hydrogel formulations, the pure

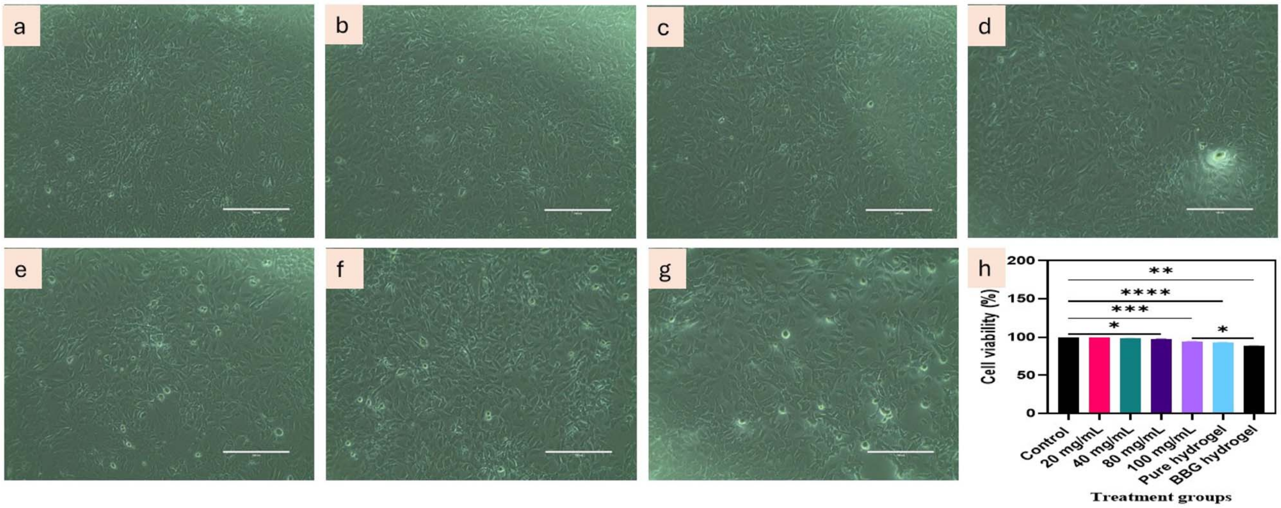

Fig. 13 Cytotoxicity assay: (a) control; (b–e) treatment with 20, 40, 80 and 100 mg per mL BBG; (f) pure hydrogel treatment, and (g) BBG-incorporated hydrogel treatment. (h) Cell viability assay.

hydrogel exhibited a hemolysis value of about 1.3%, whereas the BBG-incorporated hydrogel showed a slightly higher value of approximately 2.2%. Statistical analysis revealed significant differences between selected groups (*$p < 0.05$, **$p < 0.01$, and ****$p < 0.0001$). Despite the marginal increase shown in the BBG-incorporated hydrogel, the hemolysis values for all samples remained below the 5% threshold. Therefore, the developed hydrogel system demonstrated excellent hemocompatibility, indicating its suitability for biomedical applications involving direct blood contact, particularly as a potential hemostatic material.

12 MTT assay (cell viability)

Fig. 13 depicts the inference from the cell viability assay performed on the three hydrogels in quantitative terms. This confirms that the hydrogels have excellent cell biocompatibility with a minimum of 89% and a maximum of up to 99%. Fig. 13 depicts the images demonstrating the cell proliferation capacity of the BBG (Fig. 13b–e), xanthan gum hydrogel (Fig. 13f), BBG-incorporated hydrogels (Fig. 13g) and control (Fig. 13a). Generally, biomaterials made up of natural polysaccharides have excellent biocompatibility. The entrapment of the BBG in the hydrogel matrix decreased the hemocompatibility, yet it achieved a highly appreciable and permissible

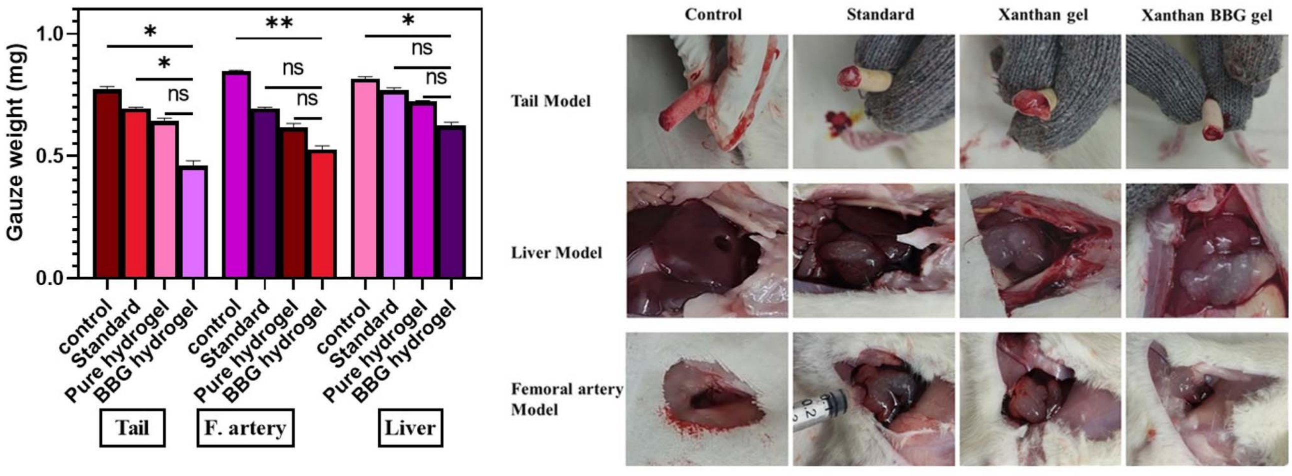

(a)

(b)

Fig. 14 (a) Gauze weight measurement for *in vivo* hemostatic evaluation. (b) *In vivo* blood clotting studies in the Wistar rat model. Error bars represent SD for $n = 3$, ** represents $P = 0.01$, and * represents $P < 0.1$.

cytocompatibility against fibroblast cells in the cell culture studies. Thus, the hydrogels can be developed further to achieve clinical translation.

13 *In vivo* haemostatic studies

The gauze measurement analysis (Fig. 14a) demonstrated that the BBG-incorporated hydrogel consistently retained a very small amount of blood. This observation emphasizes the superior haemostatic performance of the BBG-incorporated hydrogel as it effectively reduced blood loss by swiftly promoting clot formation. The enhanced haemostatic potential of the hydrogel is further supported by the reduced residual blood, which indicates efficient absorption and clot stabilization. The formation of blood clot after the application of the hydrogel is ensured by the amount of blood absorbed by the cotton gauze.

13.1 Amputated tail model

The untreated amputated tails coagulated in approximately 680 ± 20 s in the tail amputation model (Fig. 14b), which is a standard *in vivo* approach for assessing haemostatic activity. The coagulation time was reduced to 246 ± 27 s when treated with the xanthan gum hydrogel, and it was further reduced to 164 ± 10 s when treated with the BBG-incorporated hydrogel. The positive control, povidone-iodine gel, accomplished clotting within 200 ± 21 s. Both the pure xanthan hydrogel and the BBG-incorporated hydrogel composite significantly reduced bleeding time and blood loss compared to the untreated control group. The xanthan hydrogel alone demonstrated effective haemostasis, likely due to its rapid swelling and ability to absorb blood and concentrate cellular components at the injury site. The incorporation of BBG resulted in a reduction in bleeding time, which may be attributed to the release of Ca^{2+} ions that support the coagulation cascade and clot stabilization. However, the difference between the hydrogel and BBG-containing formulations remained moderate, suggesting an additive contribution of BBG to the overall haemostatic effect. This significant decrease in coagulation time with BBG-incorporated hydrogel indicates that it has a significantly greater haemostatic efficacy than the standard povidone-iodine and pure xanthan hydrogel and the positive control. This suggests that the BBG-incorporated hydrogel more effectively accelerates the intrinsic clotting process. The blood loss was absorbed and measured using cotton gauze.

13.2 Liver puncture model

The liver puncture model (Fig. 14b) offers a tightly controlled bleeding environment for the assessment of the haemostatic properties of hydrogels. In this model, the untreated liver punctures clot within 180 ± 4 s, whereas the pure hydrogel and BBG-incorporated hydrogel accomplished clotting in 103 ± 3 s and 86 ± 4 s, respectively. Clotting was observed in the positive control in 90 ± 3 s. Both the xanthan hydrogel and BBG-incorporated hydrogel effectively controlled bleeding compared to the untreated control. The hydrogel matrix rapidly absorbed blood and formed a physical barrier over the injury site, which contributed to the initial haemostatic response. The BBG-incorporated hydrogel formulation showed an improved reduction in bleeding time and blood loss, which may be associated with ionic interactions and calcium ion release that support coagulation processes. Nevertheless, the performance of the composite remained broadly comparable to that of the pure hydrogel. Even though the BBG-incorporated hydrogel and the positive control have comparable clotting times, the residual blood observed following treatment with the BBG-incorporated hydrogel was substantially reduced. The highly porous structure of the BBG-incorporated hydrogel is likely responsible for the reduction in blood loss since it helps to facilitate faster clot stabilization and absorb blood, thereby enhancing the overall haemostatic efficiency.

13.3 Femoral artery model

The femoral artery puncture model (Fig. 14b) simulates the real-time pressurized blood flow that occurs during traumatic injury, thereby providing a rigorous evaluation of haemostatic efficacy. The time required to form a stable thrombus in an untreated femoral artery is approximately 408 ± 10 s. However, pure hydrogel and BBG-incorporated hydrogel reduce this time to 270 ± 6 s and 211 ± 4 s, respectively. The positive control clots in 213 ± 7 s. However, the BBG-incorporated hydrogel exhibits the fastest clot formation, even though clotting takes longer in this model than in the liver puncture model due to the limited interaction between the hydrogel components and the swiftly flowing blood. Both the xanthan hydrogel and the BBG-containing composite demonstrated the ability to significantly reduce bleeding relative to the untreated control group. The BBG-containing hydrogel exhibited enhanced haemostatic performance, possibly due to the combined effects of the hydrogel matrix and ion release from BBG that may enhance clot formation and stabilization. However, the differences between the formulations were relatively small, indicating that the haemostatic activity is primarily governed by the hydrogel matrix, with BBG providing a supportive contribution.

The study demonstrates that BBG-incorporated xanthan gum hydrogels exhibit enhanced physicochemical and biological properties, making them highly effective for haemostatic applications. Characterization results confirmed that BBG nanoparticles possess good crystallinity, a hydrophilic nature, and colloidal stability, while their integration into the hydrogel matrix preserves essential functional groups and maintains structural integrity. The hydrogel shows excellent stability, spreadability, and injectability, which are crucial for clinical use. Swelling and degradation analyses revealed that the BBG-incorporated hydrogels absorbed more water and were degraded more slowly than pure hydrogels, indicating superior structural stability. Microbial studies highlighted strong, concentration-dependent antibacterial activity against both Gram-positive and Gram-negative pathogens, underscoring the BBG potential in infection control.

Haemostatic assays consistently show that BBG-incorporated hydrogels significantly accelerated clotting time, reduced the blood coagulation index, and promoted robust RBC aggregation and platelet adhesion, surpassing both controls and pure hydrogels. Coagulation tests confirmed the activation of both intrinsic and extrinsic pathways, which was supported by reduced PT and aPTT values. D-dimer levels and haemolysis assays further affirmed effective clot formation without excessive fibrinolysis or RBC lysis, ensuring blood compatibility. Cell viability studies revealed excellent cytocompatibility, suggesting safety for wound healing. *In vivo* models validated that the BBG-incorporated hydrogels minimized blood loss and accelerated clot formation in traumatic bleeding scenarios, outperforming standard treatments. Collectively, these results confirmed that BBG-incorporated hydrogels are promising candidates for rapid and haemorrhage control.

14 Conclusion

This study shows that adding BBG to a hydrogel matrix significantly improves its ability to stop bleeding. The BBG-incorporated hydrogel showed a far better RBC aggregation and platelet adhesion than the pure hydrogel and control groups. This reflects enhanced blood cell interactions, which are important for the quick formation of clots. The lack of aberrant fibrinolysis is corroborated by the decreasing values of both PT and aPTT as the composite concentration increased, with BBG-incorporated hydrogel demonstrating the most significant decline. Coagulation tests showed that D-dimer levels remained approximately the same. The swelling-degradation research also showed that the BBG-incorporated hydrogel absorbed more water and broke down more slowly than the pure hydrogel, indicating that it was more structurally stable. These results collectively confirmed that the haemostatic efficacy, stability, and usefulness of the hydrogel were improved by the inclusion of BBG, making it a promising candidate for expedited wound treatment and haemorrhage control applications. This study demonstrates that the chemical composition and dissolution behaviour of borate bioglass play a central role in governing the structure–property–function relationships of xanthan-based hemostatic hydrogels.

Ethical statement

All animal procedures were performed in accordance with the guidelines established by the Committee for the Purpose of Control and Supervision of Experiments on Animals (CPCSEA) and approved by the Institutional Animal Ethics Committee (IAEC) of SRM Institute of Science and Technology. Human blood was drawn from healthy volunteers in compliance with the Declaration of Helsinki and relevant national laws and approved by Institutional Ethical Committee at SRM Medical College hospital and Research Centre. Informed consents were obtained from human participants of this study.

Author contributions

VS-formal analysis, writing – original draft. MSM-formal analysis, writing – original draft, visualization and data curation. VS-formal analysis, writing – review & editing. BP-formal analysis, validation, visualization. DVG – conceptualization; supervision, validation, writing – review & editing.

Conflicts of interest

The authors have no conflicts to disclose.

Data availability

The data that support the findings of this study are available from the corresponding author upon reasonable request.

Acknowledgements

The authors Vanshika Singh and Dr G. Devanand Venkatasubbu thank Nanotechnology Research Centre and SCIF, Department of Physics and Nanotechnology, SRMIST, for providing the characterization facilities.

References

1 E. W. Davie and O. D. Ratnoff, *Science*, 1964, **145**, 1310–1312.
2 D. M. Monroe and M. Hoffman, *Arterioscler. Thromb. Vasc. Biol.*, 2006, **26**, 41–48.
3 Z. M. Ruggeri, *Nat. Med.*, 2002, **8**, 1227–1234.
4 N. Mackman, *J. Thromb. Haemostasis*, 2008, **6**, 303–305.
5 S. A. Smith, R. J. Travers and J. H. Morrissey, *Crit. Rev. Biochem. Mol. Biol.*, 2015, **50**, 326–336.
6 M. Hoffman and D. M. Monroe, *Thromb. Haemost.*, 2001, **85**, 958–965.
7 C. Esmon, *Biochim. Biophys. Acta*, 2000, **1477**, 349–360.
8 H. Spronk, J. Govers-Riemslag and H. ten Cate, *BioEssays*, 2004, **25**, 1220–1228.
9 M. P. Chapman, E. E. Moore, H. B. Moore, E. Gonzalez, A. P. Morton, J. Chandler, C. D. Fleming, A. Ghasabyan, C. C. Silliman, A. Banerjee and A. Sauaia, *J. Trauma Acute Care Surg.*, 2015, **79**, 925–929.
10 H. Weng, W. Jia, M. Li and Z. Chen, *Carbohydr. Polym.*, 2022, **294**, 119767.
11 S. López Esteban, E. Saiz, S. Fujino, T. Oku, K. Suganuma and A. Tomsia, *J. Eur. Ceram. Soc.*, 2003, **23**, 2921–2930.
12 F. Chen, X. Cao, X. Chen, J. Wei and C. Liu, *J. Mater. Chem. B*, 2015, **3**, 4017–4026.
13 D. Ege, K. Zheng and A. R. Boccaccini, *ACS Appl. Bio Mater.*, 2022, **5**, 3608–3622.
14 J. Jones, *Acta Biomater.*, 2013, **9**(1), 4457–4486.
15 J. Gilabert-Porres, S. Martí, L. Calatayud, V. Ramos, A. Rosell and S. Borrós, *ACS Appl. Mater. Interfaces*, 2016, **8**, 64–73.
16 J. Xue, T. Wu, Y. Dai and Y. Xia, *Chem. Rev.*, 2019, **119**, 5298–5415.
17 R. Patel, M. M. Tosif, O. A. Alsaidan and B. Prajapati, *Carbohydr. Polym.*, 2025, **366**, 123914.
18 D. M. Monroe and M. Hoffman, *Arterioscler. Thromb. Vasc. Biol.*, 2006, **26**, 41–48.
19 S. Tabasum, A. Noreen, A. Kanwal, M. Zuber, M. N. Anjum and K. M. Zia, *Int. J. Biol. Macromol.*, 2017, **98**, 748–776.

20 A. Stanzione, A. Polini, V. La Pesa, A. Romano, A. Quattrini, G. Gigli, L. Moroni and F. Gervaso, *Appl. Sci.*, 2020, **10**, 6550.

21 F. Z. Kocak, M. Yar and I. U. Rehman, *Biotechnol. Bioeng.*, 2024, **121**, 2767–2779.

22 G. L. da Silva, I. F. Rodrigues, S. S. S. Pereira, G. M. G. Fontoura, A. S. Reis, F. Pedrochi and A. Steimacher, *J. Non-Cryst. Solids*, 2022, **595**, 121829.

23 O. S. Adeyemi, E. O. Shittu, O. B. Akpor, D. Rotimi and G. E. Batiha, *EXCLI J.*, 2020, **19**, 492–500.

24 H. Huang, R. Xu, P. Ni, Z. Zhang, C. Sun, H. He, X. Wang, L. Zhang, Z. Liang and H. Liu, *Mater. Today Bio*, 2022, **16**, 100369.

25 A. D. Peshkova, E. K. Rednikova, R. R. Khismatullin, O. V. Kim, V. R. Muzykantov, P. K. Purohit, R. I. Litvinov and J. W. Weisel, *Blood Adv.*, 2025, **9**, 3418–3428.

26 M. Ms and G. D. Venkatasubbu, *ACS Appl. Bio Mater.*, 2024, **7**, 6998–7008.

27 R. Chen, Y. Hao, S. Francesco, X. Mao and W.-C. Huang, *Mar. Life Sci. Technol.*, 2023, **6**, 115–125.

28 C. B. Jha, C. Singh, P. Patil, K. Manna, S. Singh, R. Varshney and R. Mathur, *Nanotechnology*, 2023, **35**, 095102.

29 K. S. Venkataprasanna, J. Prakash, S. Vignesh, G. Bharath, M. Venkatesan, F. Banat, S. Sahabudeen, S. Ramachandran and G. Devanand Venkatasubbu, *Int. J. Biol. Macromol.*, 2020, **143**, 744–762.

30 H. Su, S. Wei, F. Chen, R. Cui and C. Liu, *RSC Adv.*, 2019, **9**, 6245–6253.

31 B. M. Mohammed, D. M. Monroe and D. Gailani, *Platelets*, 2020, **31**, 417–422.

32 Y. Wang, Y. Guo, Y. Liu, X. Zhao, Y. Huang, X. Zhang, X. Hu, K. Mequanint, G. Luo and M. Xing, *Adv. Healthcare Mater.*, 2024, **13**, 2304523.

33 Z. Karahaliloğlu, M. Demirbilek, İ. Ulusoy, B. Gümüşkaya and E. Baki Denkbaş, *J. Appl. Polym. Sci.*, 2016, **133**, 43657.